An Ultrawideband (35:1) Shared-Aperture Antenna Array With Multihyperuniform Disorder

Orestis Christogeorgos, Ernest Okon, *Member, IEEE*, and Yang Hao, *Fellow, IEEE*

***Abstract*— This article is aimed at studying the concept of multihyperuniformity and applying it to the design of shared-aperture antenna arrays for ultrawideband, broadside unidirectional emission. In this study, we present our work on the design of multiple frequency helical antenna arrays within a shared-aperture configuration, incorporating multihyperuniform disorder. The array consists of seven different intercalated helical subarrays and is optimized to cover a 35:1 continuous bandwidth at 0.4–14 GHz. We provide comprehensive details regarding the fabrication process and present measurement results. Our work provides a new alternative to existing solutions of antenna array designs and has wider applicability in electromagnetics. The proposed methodology extends the limitations for the realization of multiband antenna arrays, surpassing the previously reported designs that operated in a maximum of three frequency bands, by incorporating naturally optimized disordered distributions.**

***Index Terms*— Helical antenna, multihyperuniform disorder, shared-aperture antenna arrays, ultrawideband arrays.**

I. Introduction

THERE have been many studies in the design of wideband/broadband antenna arrays that are compact and low profile. One example is the closely coupled antenna arrays, which consist of interconnected antenna elements that are distributed in a periodic format. The operating principle of these arrays is associated with the constructive use of mutual coupling occurring between neighboring elements in close proximity, which leads to an increase in the array's operating bandwidth. Some of the first efforts toward applying the concept is a linear array of five connected stripline notch antennas [1], as well as a 9×9 interconnected array of bunny-ear elements [2], both operating in a 5:1 bandwidth. In [3], the concept of employing capacitances between the tips of neighboring planar antenna elements, in order to control their mutual coupling, was introduced for the first time, thus paving the way for the design of planar closely coupled broadband antenna arrays. Some example designs that employ this technique include a 8×8 planar dipole array with interdigital capacitors operating in a 9:1 bandwidth [4] and a 9×9 closely coupled bowtie array, which operates in a 21:1 bandwidth [5].

Another approach to designing broadband antenna arrays is through the use of multiband intercalated shared-aperture antenna arrays, which consist of different types of elements interleaving with each other in a periodically ordered format, and therefore, multiple bandwidths of the radio spectrum can be covered with one compact design. The design complexity of such arrays is notably high, primarily due to the challenge of preventing antenna element overlaps across different subarrays. This challenge arises from the necessity of maintaining a fixed interelement spacing in periodic distributions to achieve radiation patterns free from grating lobes.

One of the first shared-aperture antenna array designs was the dual-band antenna array presented by Pozar and Targonski [6], where the low-band elements are perforated so that some of the high-band array elements reside within the perforations and thus avoid any element overlaps. Since then, several notable efforts have been made toward the evolution of the idea of multiband shared-aperture antenna arrays. A more recent design that resembles this approach is presented in [7], where a dual-band array of circular patches is designed with the low-frequency antennas having perforations on their edges in order to accommodate the antenna array operating at high frequencies over the same aperture. In [8], a dual-band array of self-similar interleaving folded dipoles is presented. This design principle was also employed in the triband antenna array [9], where the low-band array consists of perforated square patches, the mid-band array consists of cross patches, and the high-band array consists of regular square patches, all etched over the same substrate. Similarly, Chang et al. [10] utilized a comparable approach by interleaving a high-band patch antenna array with a low-band patch antenna array, enabling dual-band operation specifically for oblique beam-steering angles.

Other approaches include a dual-band integrated design [11], [12] or a novel technique [13], where the low-band elements are designed as fragmented patches while operating as a 2×2 array at the high-band frequencies, thus leading to a dual-band antenna array. The other widely used technique involves stacking various antenna arrays on separate dielectric substrates, creating a layered configuration. During

Manuscript received 20 October 2023; revised 10 May 2024; accepted 18 May 2024. Date of publication 4 June 2024; date of current version 9 July 2024. The work of Orestis Christogeorgos was supported in part by Engineering and Physical Sciences Research Council (EPSRC) under Grant 2272076 and in part by Thales U.K. The work of Yang Hao was supported in part by the IET AF Harvey Research Prize; in part by EPSRC under Grant EP/R035393/1, Grant EP/W026732/1, and Grant EP/X02542X/1; and in part by the Royal Academy of Engineering. *(Corresponding author: Yang Hao.)*

Orestis Christogeorgos and Yang Hao are with the School of Electronic Engineering and Computer Science, Queen Mary University of London, E1 4NS London, U.K. (e-mail: o.christogeorgos@qmul.ac.uk; y.hao@qmul.ac.uk).

Ernest Okon is with Thales U.K., RH10 9HA Crawley, U.K. (e-mail: ernest.okon@uk.thalesgroup.com).

Color versions of one or more figures in this article are available at https://doi.org/10.1109/TAP.2024.3406040.

Digital Object Identifier 10.1109/TAP.2024.3406040

this design process, it is crucial to ensure that the top-layer array exhibits transparency at the operating frequencies of the antenna arrays given next. Simultaneously, the antenna arrays below should be designed to be fully reflective at the operating frequencies of the antenna arrays above, effectively acting as a ground. The underlying theory is that these planar arrays can be regarded as frequency-selective surfaces (FSSs). Since the FSS are inherently narrowband, this approach is often restricted to multiband array designs with low-frequency ratios, which in most cases are limited to the design of dual-band arrays [14], [15], [16], [17], [18], [19]. A more intricate method is developed to design stacked triband antenna arrays, where one type of element is designed to resonate at its corresponding operating frequency, whereas it acts as an FSS at the other operating frequencies [20], [21], [22], [23].

The design of shared-aperture antenna arrays is a complex and challenging task that involves optimizing numerous interconnected parameters. In previous design approaches, a common factor among them all is the utilization of periodic array distributions. This greatly limits the design degrees of freedom, due to the fixed interelement spacing that is required to achieve grating lobe-free radiation patterns. This is also the reason behind the absence of any reported work in the existing literature of more than three different arrays in an interleaved shared-aperture array design. As such, it becomes evident that in order to further enlarge the operating bandwidth of shared-aperture antenna arrays and to be able to cover more operating frequency bands with a single compact design, optimized aperiodic distributions need to be employed so that the grating lobes are suppressed for all frequency bands of interest, while at the same time, the employed elements will not overlap with other elements in the distribution.

For the past 20 years, researchers have been studying a unique type of distribution found in many natural and biological systems, that is, hyperuniform disordered. Such a system is statistically isotropic with no Bragg peaks, such as a liquid, while exhibiting suppressed large-scale density fluctuations, such as a crystal [24]. Examples include the receptors organized in a well-adapted immune system [25] or the photoreceptors that can be found on the retina of avian eyes [26]. Furthermore, several standard cosmological models have been found to be "super-homogeneous" [27], [28], which is an early term that was used to describe hyperuniform disorder.

Due to their unique physical properties, hyperuniform disordered systems have been applied extensively in the fields of material science and wave physics. In particular, this type of point distribution has been deployed in order to overcome the Bragg diffraction that is intrinsic to periodic structures. In [29], the effect of hyperuniformity in composite materials was investigated, which led to the design of a hyperuniform disordered Luneburg lens that has low radar cross section [30]. Furthermore, antenna arrays with hyperuniform disorder have been demonstrated to overcome physical limits, such as bandwidth and induced grating lobes, which are typically encountered by periodic arrays. Christogeorgos et al. [31] introduced a 16-element Vivaldi antenna array with hyperuniform disorder that suppresses the grating lobes that the equivalent 4×4 periodic array suffers from, whereas in [32], a reconfigurable reflectarray with hyperuniform disorder is shown to have identical performance with an equivalent reconfigurable periodic reflectarray, but with 36% less elements required. The idea is also applied to the design of scattering reduction metasurfaces, which can be made polarization independent [33]. In addition, this type of distribution has been applied in the field of photonic crystals, where hyperuniform disordered systems are employed to design complete bandgaps and subsequently high-Q optical cavities and free-form photonic waveguides [34], [35], [36], [37]. Extraordinary directive emission properties were also observed in hyperuniform disordered terahertz lasing devices [38], as well as in a gold plasmonic surface characterized by hyperuniform disorder, where a single broad scattering resonance governs both the annular far-field light scattering and directional emission [39].

Therefore, the increasing popularity of hyperuniformity in the realm of electromagnetics as a superior choice over periodic or other forms of aperiodic distributions has now become evident. Here, drawing inspiration from the photoreceptor arrangement found on the retina of avian eyes, we apply a new concept of multihyperuniform disorder, to design shared-aperture antenna arrays, where each point distribution is associated with different intercalated hyperuniform arrays operating at different frequency bands, for multiband or broadband applications. As such, our proposed methodology is different from previously published work on hyperuniform antenna arrays where single hyperuniform distributions are employed for wideband sidelobe suppression, albeit in a single-frequency band. The proposed methodology can also be regarded as a multiscale packing problem in which an ordered/periodic system would fail and a random system would require computationally intensive optimization. Here, we present the hepta-band multihyperuniform helical array that is optimized to cover a 35:1 fractional bandwidth with directive radiation pattern, suppressed grating lobes, and steadily increasing high realized gain over the whole frequency bandwidth while avoiding any element overlaps, which would not be possible by employing periodic distributions.

This article is dedicated to describing the design process of applying multihyperuniformity in the field of shared-aperture antenna arrays and is structured as follows. Section II is dedicated to briefly introduce the basics of hyperuniform disordered distributions and the rationale behind applying multihyperuniformity in the field of shared-aperture antenna arrays. Section III provides technical details on the employed antenna elements and provides insights into various design considerations, shedding light on the necessary tradeoffs, and compromises when applying the multihyperuniform distribution in the shared-aperture antenna array. Section IV presents the proof-of-concept design and the measurement results for the fabricated hepta-band multihyperuniform helical array, while Section V is dedicated to comparing the proposed design with other existing state-of-the-art multiband shared-aperture antenna arrays. Finally, Section VI concludes the work and discusses future design considerations.

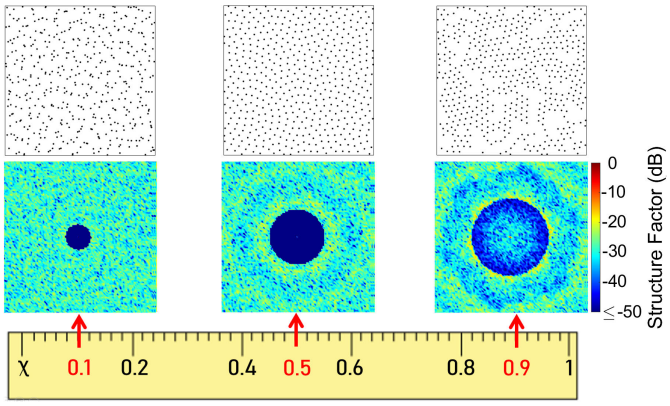

Fig. 1. Hyperuniform distributions of 500 circular disks distributed over the same aperture area for different values of the stealthiness parameter χ. Top: resulting distributions. Middle: corresponding structure factor plots. Bottom: stealthiness parameter range with indications of the corresponding value for each distribution. From left to right, the distributions have a stealthiness parameter equal to 0.1 (disordered regime), 0.5 (wavy crystalline regime), and 0.9 (crystalline regime).

II. Multihyperuniform Distributions

Hyperuniform distributions are known to have short-range crystal-like and long-range liquid-like pair correlations [24]. As such, the nearest neighbors in a hyperuniform disordered point distribution are situated at fixed distances, whereas the second, third, and so on nearest neighbors are randomly distributed [31]. In turn, this indicates that the structure factor representing the point pattern diminishes within a circular region surrounding the origin in reciprocal space. The structure factor is a function that is proportional to the scattered intensity of radiation from a system of points, and for this reason, it is also referred to as the scattering pattern. For a configuration of N points residing within a square area of sidelength L at positions $\mathbf{r}_1$, $\mathbf{r}_2$, ..., $\mathbf{r}_N$, the structure factor is defined as

$$S(\mathbf{k}) = \frac{1}{N}\left|\sum_{j=1}^{N} e^{i\mathbf{k}\cdot\mathbf{r}_j}\right|^2 \tag{1}$$

where $\mathbf{k}$ is an appropriate infinite set of wave vectors. The radius of the circular exclusion region around the origin for which the structure factor diminishes is a positive integer termed K. This radius is associated with the amount of disorder/order in the resulting distribution, leading to a special type of hyperuniform disordered distributions that are termed as stealthy [40], [41]. In order to quantify the amount of disorder/order in such an N-particle system, each resulting pattern is characterized by the stealthiness parameter $\chi = M(K)/2N$, where $M(K)$ is equal to the number of wavevectors that reside within the circle of radius K in reciprocal space and is termed as the number of constrained degrees of freedom. In order to generate hyperuniform and multihyperuniform distributions, we employ the computational model that is formulated in [42], where the process for calculating $M(K)$ is also described.

The stealthiness parameter ranges from 0 to 1 and three distinct regimes for the final configurations as χ varies have been observed [43]: the disordered, wavy crystalline, and crystalline regimes, where the χ value belongs in the low end, the middle end, and the upper end of the disorder/order spectrum, respectively. The χ range for which the distribution belongs in the wavy crystalline regime increases with the number of elements [43]. Employing the same geometric parameters (i.e., the number and size of points and aperture area), but tuning the χ parameter, leads to the emergence of different distributions and structure factor patterns. An example of this can be seen in Fig. 1, where 500 circular disks of the same size are distributed over the same aperture area, but with different χ parameter values. The top illustrates the resulting distributions, whereas the bottom illustrates the corresponding structure factor behavior. As it can be seen, when χ is in the wavy crystalline regime, the structure factor is minimized within the circular exclusion region. However, when χ is in the crystalline regime of the disorder/order spectrum, the structure factor values within the circular region become large compared to the disordered and wavy crystalline distributions.

When antenna elements are integrated and the principles of hyperuniform disorder are applied, it has been demonstrated that the resulting radiation pattern of the array exhibits behavior akin to the structure factor. This leads to the suppression of grating lobes across a broad spectrum of frequencies and various beam-steering angles [31], [32]. In addition, research has revealed the existence of optimal combinations involving the number of elements used and the corresponding stealthiness parameter for such a distribution. As the number of elements in the array increases, the ideal value for the stealthiness parameter converges around 0.5, which positions it at the midpoint of the disorder-to-order spectrum. Furthermore, the size of the radiation pattern exclusion region (denoted as θ_{exc}) of an array of radiation sources is interconnected with the operating wavelength (λ), the side length of the square aperture area (L), and the selected radius (K) of the structure factor exclusion region, as detailed in [31]

$$\theta_{exc} = \arcsin\left(\frac{\lambda}{L}\sqrt{K}\right). \tag{2}$$

Multihyperuniform distributions are a special case of hyperuniform systems that have been found in several natural systems. This type of distribution consists of separate hyperuniform distributions of elements, all within the same computational domain. Each separate distribution is termed as species and the overall distribution is hyperuniform as well, hence the term multihyperuniformity [25], [26]. In particular, it has been found that the photoreceptor system on avian eye retina follows such a disordered multielement distribution and each photoreceptor species is associated with sampling different parts of the optical spectrum. As such, avian vision is highly directive and enables for sampling parts of the ultraviolet (UV) spectrum, which other animals are not able to see, due to the corresponding crystalline arrangement of the photoreceptors. We apply the concept in the field of shared-aperture antenna arrays to design, fabricate, and test a helical array made of seven different intercalated arrays, each operating at different frequency bands, that follow a multihyperuniform distribution. An example of such a distribution is shown in Fig. 2, with the top illustrating the species distribution and the bottom illustrating the corresponding structure factor plots.

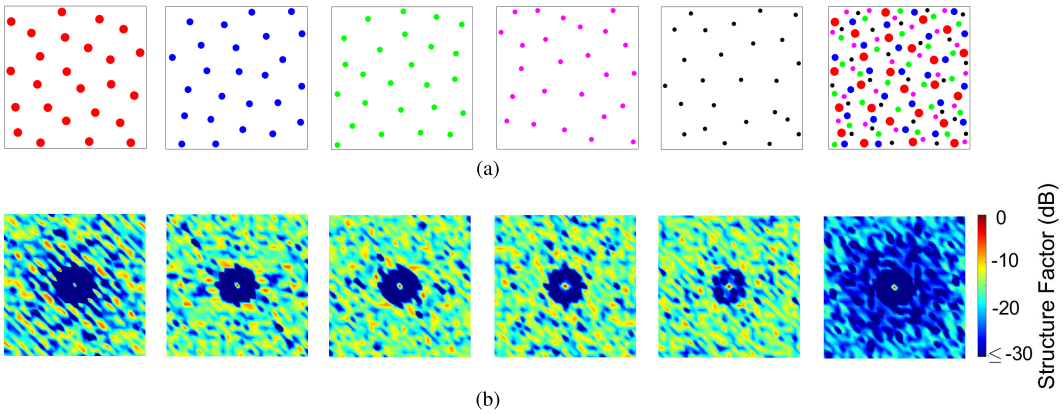

Fig. 2. Multihyperuniform distribution of circular particles with varying diameter. Each particle arrangement, termed as species, follows a hyperuniform distribution and the overall distribution of particles is hyperuniform as well. (a) Hyperuniform distributions of five different species and the overall multihyperuniform distribution are shown in the rightmost panel. (b) Corresponding structure factor of each species. The rightmost panel illustrates the structure factor behavior of the overall distribution. Each corresponding structure factor is stealthy hyperuniform and the overall structure factor is also stealthy hyperuniform.

The rightmost panel indicates that the overall distribution is hyperuniform as well.

III. Design and Fabrication of the Helical Array With Multihyperuniform Disorder

A. Element Design

As it is understood, a hyperuniform distribution can be advantageous for reducing the sidelobe levels and enhancing the gain of an antenna array across a wide frequency range when the constituent elements emit signals toward the central direction of the array. Intuitively, we should use wideband unidirectional antenna elements to create a multihyperuniform ultrawideband antenna array. Therefore, for our conceptual multihyperuniform array design, we select the helical antenna element operating in the axial mode as the radiating component without loss of generality. The helical antenna operating in the axial mode operates in a 1.8:1 continuous frequency bandwidth with unidirectional radiation pattern and high realized gain. The operating frequency of the axial mode helical antenna is associated with its diameter and the spacing between its turns [44].

To fabricate helical antennas, we use the stereolithography (SLA) 3-D printing technology and in particular the Form 3+ printer and white photopolymer resin, both from Formlabs as the printing material. We have tested the dielectric properties by using the 85072A 10-GHz split cylinder resonator from Keysight, which resulted in the relative permittivity being $\epsilon_r \approx 2.76$ and the loss tangent $\tan\delta \approx 0.0046$. The 3-D printed dielectric supports are printed with corrugations at the positions where the helical antenna wires are wounded, allowing for precise fabrication of the helical antennas. Thus, these 3-D printed supports provide rigidity to the helical structures, and meanwhile, they help with size reduction of the helical antennas and the corresponding array aperture due to the dielectric loading.

Since the Formlabs Form 3+ printer has a maximum x and y sidelength of 145 mm, the lowest frequency helical antenna will have a radius of $R = 67.625$ mm. Our objective is to achieve coverage across a continuous frequency bandwidth. Consequently, the lowest operating frequency of the subsequent helical subarray, referred to as "species," will be set to match the highest operating frequency of the preceding species, and this pattern will continue. It is apparent that the lowest frequency operating elements will have the largest diameter and spacing between their turns since both are dependent on the operating wavelength for axial mode operation. As such, in order to maintain the height of the overall array as short as possible, we design the lowest operating helical antenna with only one turn. All elements have the same height, and thus, the number of turns for each element will be determined accordingly. Therefore, for higher operating frequencies, a more number of turns are employed for each helix, leading to higher gain values and directivity. On the other hand, increasing the number of turns for the higher frequency helical elements increases their electrical height and as such leads to the decrease of their radiation efficiency. Nevertheless, in this work, our aim is to illustrate how the multihyperuniform distribution can be employed for

TABLE I
Essential Geometrical Parameters of the Helical Antenna Elements Employed for the Multihyperuniform Array. Each Helical Antenna Type Is Termed as "Species" With Lower Species Number Indicating Lower Operating Frequencies. D Is the Helix Diameter, S Is the Spacing Between Its Turns, NofT Is the Number of Turns, and f_{low} and f_{high} Are the Lowest and Highest Operating Frequencies, Respectively, for Axial Mode Operation

Species no.	D (mm)	S (mm)	$NofT$	f_{low} (GHz)	f_{high} (GHz)
1st	135.25	101.98	1	0.4	1
2nd	70.51	53.17	1.92	1	1.7
3rd	38.94	29.36	3.47	1.7	2.8
4th	22.66	17.09	6	2.8	4.5
5th	13.4	10.1	10	4.5	6.4
6th	9.27	7	14.6	6.4	10
7th	5.85	4.41	23.12	10	14

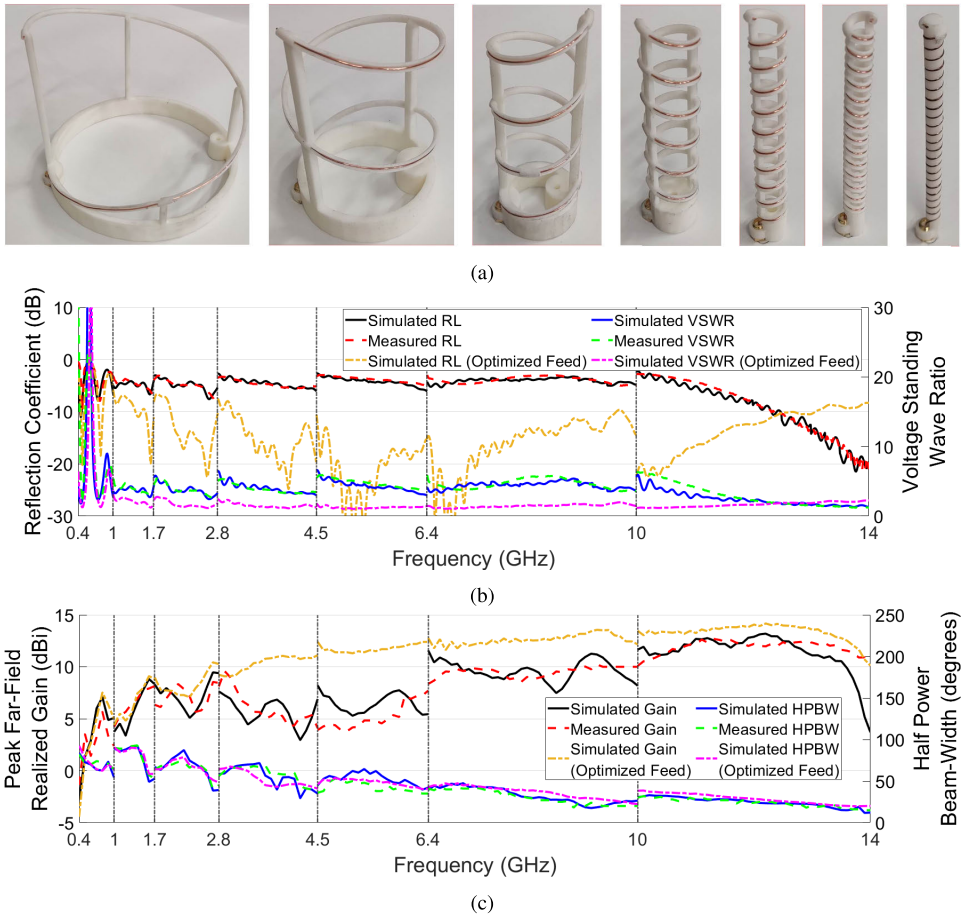

Fig. 3. (a) Fabricated helical antenna elements. Each type of helical antenna is termed as "species," and from left to right, the 1st–7th species are shown, which are designed to operate in the 0.4–1-GHz, 1–1.7-GHz, 1.7–2.8-GHz, 2.8–4.5-GHz, 4.5–6.4-GHz, 6.4–10-GHz, and 10–14-GHz band, respectively. Consecutive species have opposite turn directions in order to minimize the mutual coupling in the multihyperuniform array design. (b) Measured, simulated, and simulated with optimized feed RL and VSWR results for the seven different species shown in (a). (c) Measured, simulated, and simulated with optimized feed peak far-field realized gain and HPBW results for the seven different species shown in (a). The vertical dotted lines indicate the transition between operating bandwidths of consecutive species.

ultrawideband high-gain unidirectional emission arrays, and as such, we design our helical elements to have an increased number of turns as the operating frequency increases. Table I presents the results of the aforementioned process, where the essential geometrical parameters of the seven different helical antennas that will be used in the multihyperuniform array are tabulated, along with the corresponding operating frequency bands. As it can be seen, the elements can cover a continuous 35:1 fractional bandwidth.

Finally, in order to ensure that the helical antennas are operating in axial mode at the intended frequency bandwidths, we simulated each helical antenna using CST Microwave Studio and proceeded in fabricating these antennas [see Fig. 3(a)]. It is important to note that the fabricated helical elements are driven by an SMA connector with 50-Ω characteristic impedance. In our simulations, we drive the helical elements with feeds that are optimized to match the individual elements to 50-Ω at the corresponding operating frequency bands. On the other hand, when fabricating the array, we found out that the employed SMA connectors affect the impedance matching behavior of the elements. As such, we introduced into our simulations the SMA connectors that were employed for feeding the fabricated elements and observed the impedance matching behavior. The results of this can be seen in Fig. 3(b), where the vertical dotted lines indicate the transition between operating bandwidths of consecutive species. As it can be seen from our two different sets of simulation results, the helical antennas with optimized feeds have improved impedance matching performance compared to the fabricated elements, and in most cases, the reflection coefficient (RL) is below the usual requirement of −10 dB. We also measured the elements' radiation patterns in an anechoic chamber. As it is expected, the poor impedance matching behavior of the fabricated helical elements results in lower realized gain values as can be evidenced in Fig. 3(c), where the peak far-field realized gain and the half-power beamwidth (HPBW) of all elements are illustrated. The lower frequency helices consist of few turns, and as such, although the impedance matching behavior of the elements with optimized feeds is improved, the increase to the peak far-field realized gain (≈1 dB) is not as significant as for higher frequency helices. On the other hand, for elements with more number of turns, a greater increase (≈5 dB) to the realized gain can be observed for the case where optimized feeds are

employed. It is interesting to note that the HPBW of the elements remains almost identical when optimized feeds are employed.

The measured and simulated results for the case where the feeds are not optimized for 50-Ω impedance matching generally agree with each other, with minor discrepancies observed. In particular, for the 1st–7th species elements, the average difference between the simulated and measured peak far-field realized gain is 1.9, 0.8, 1.2, 1.3, 1.8, 0.9, and 1 dB in the corresponding operating frequency bands. The maximum difference is observed at 14 GHz, for the 7th species element with the difference being 6.4 dB. It is observed that for some frequencies, the measured gain of the helical antenna elements is higher than the simulated gain and this is attributed to four main reasons: 1) slight misalignments of the standard gain antenna during our gain measurements; 2) discrepancies between the measured dielectric properties of the supporting material against the actual dielectric properties at the overall frequency band of interest; 3) minor inaccuracies in the modeling of the SMA-to-helix transition in our simulations; and 4) coarse mesh density in our simulations, where a finer mesh could not be obtained with the computing resources at hand.

Nevertheless, although there exist some slight discrepancies between the measured and simulated gain values, the fabricated helical elements have unidirectional radiation patterns with the peak realized gain over 5 dBi over most of the 0.4–14-GHz bandwidth and thus can be employed for our proof-of-concept demonstration of the ultrawideband shared-aperture array with multihyperuniform disorder. Furthermore, as it was expected, the helical antennas with a larger number of turns have more directive beams and higher peak realized gain. Finally, as it is well known, helical antennas operating in the axial mode have poor impedance matching performance [45], [46], [47] with usual RL values ranging around −5 dB, while better impedance matching can be achieved with an increase to the number of turns. This is also evident in this work, as Fig. 3(b) suggests where the measured and simulated RL and voltage standing wave ratio (VSWR) of the fabricated elements are given. In the existing literature, there have been reported some techniques to match the impedance of a fabricated helical antenna to 50 Ω by employing a quarter wavelength transformer and applying stub matching techniques [47], [48]. In this article, since our focus is to demonstrate the concept of multihyperuniform disorder in the design of shared-aperture antenna arrays, we will not put any additional effort in improving the impedance matching behavior of the fabricated helical antenna elements.

B. Multihyperuniform Shared-Aperture Helical Array Design

In order to determine the multihyperuniform distribution in the shared-aperture antenna array design, several factors need to be considered, such as the array aperture and the number of elements for each species. As it can be understood, since these parameters are intertwined, a compromise needs to be made with regard to the array's performance, its overall size, and the number of elements to be employed. The employed helical antenna elements are designed to cover a continuous bandwidth in the 0.4–14-GHz range and the square aperture sidelength is chosen to be $L = 460$ mm, which is equal to 0.6λ and 21.5λ at the lowest and highest operating frequencies of 0.4 and 14 GHz, respectively.

Since the lower frequency elements are the largest ones and in order to maintain the aperture as small as possible, we only employ four elements for the 1st species and arrange them periodically in a 2×2 distribution, as shown in Fig. 4(a). A parametric study for the 1st species interelement spacing showed that a distance of 0.8λ at the highest corresponding operating frequency of 1 GHz is optimal for obtaining the highest peak far-field realized gain, maintaining low sidelobe levels, and leaving enough space for the rest of the elements to be distributed.

The size of the 2nd species elements also leads to using only five elements and arranging them periodically by employing a cross distribution, as shown in Fig. 4(b). A similar parametric study for the 2nd species interelement spacing showed that a distance of 0.8λ at the highest corresponding operating frequency of 1.7 GHz is optimal for obtaining the highest peak far-field realized gain, maintaining low sidelobe levels, and avoiding element overlaps with the already distributed 1st species elements. The first two arrays take up most of the space in the shared-aperture array distribution, and thus, we can no longer apply a periodic distribution for the next arrays while avoiding element overlaps. As such, for the rest of the subarrays to be distributed, we employ hyperuniform disordered distributions.

To design the multihyperuniform antenna array, we may choose point distributions with different structure factor behaviors. This process is somehow similar to the conventional antenna array design, where different element distributions can be found to manipulate sidelobes and beam patterns. They include Chebyshev, Taylor, or binomial distributions. Radiation patterns of hyperuniform disordered arrays can be described by a unique quantity termed as "exclusion region" that surrounds the main lobe, where the level of sidelobes can be maintained to be extremely low. By employing (2), we can choose the stealthiness parameter and the number of elements for each species so that the radiation pattern exclusion region will have a predetermined size θ_{exc} at the operating frequencies of interest.

Furthermore, for generating hyperuniform distributions, there exist optimal pairs of (N, χ) values for the number of elements and the stealthiness parameter (see [31, Fig. 2]), which can lead to the desired θ_{exc}. Generally, for $\theta_{exc} \in (10°, 35°)$, the resulting radiation patterns are highly directive with the directivity increasing as θ_{exc} decreases. However, from the aforementioned process, it can be understood that low θ_{exc} values lead to an increased number of elements. Having these considerations in mind and by employing the aforementioned methodology, we were able to determine the number of elements for each array and the results of this process are tabulated in Table II. In order to generate the hyperuniform distributions while maintaining the optimal (N, χ) combinations and avoiding element overlaps, we employ the computational model presented in [42]. Our design leads to a total packing fraction (available aperture area that is

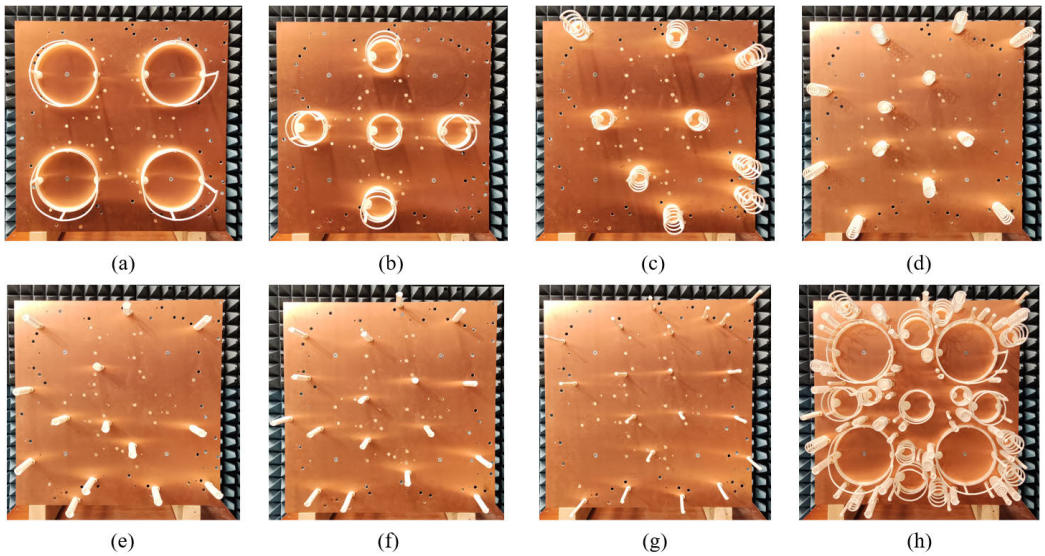

Fig. 4. Multihyperuniform distribution of seven helical arrays (species) over the same aperture area. (a) 1st species. (b) 2nd species. (c) 3rd species. (d) 4th species. (e) 5th species. (f) 6th species. (g) 7th species. (h) Overall multihyperuniform distribution.

TABLE II

DISTRIBUTION PARAMETERS FOR THE MULTIHYPERUNIFORM DISTRIBUTION SHOWN IN FIG. 4. θ_{exc} IS THE EXCLUSION REGION RADIUS IN THE RADIATION PATTERN AT THE CENTRAL OPERATING FREQUENCY ($f_{central}$), N IS THE NUMBER OF ELEMENTS FOR EACH ARRAY DISTRIBUTION, AND χ IS THE CORRESPONDING STEALTHINESS PARAMETER ASSOCIATED WITH EACH HYPERUNIFORM DISTRIBUTION

Species no.	θ_{exc} (degrees)	$f_{central}$ (GHz)	N	χ
1st	–	0.7	4	–
2nd	–	1.4	5	–
3rd	35	2.3	9	0.3
4th	23	3.7	12	0.38
5th	21	5.5	14	0.4
6th	14	8.2	17	0.41
7th	11	12	20	0.44

occupied by the elements) of around 60%. Moreover, in order to decouple the different species as much as possible and to decrease the undesired out-of-band mutual coupling in the multihyperuniform antenna array design, the helical elements of consecutive species have opposite directions for their turns, as can be evidenced in Fig. 3(a), that is, the 1st, 3rd, 5th, and 7th species' turns are right-handed, whereas the 2nd, 4th, and 6th species' turns are left-handed.

IV. ARRAY SIMULATION AND MEASUREMENT RESULTS

The multihyperuniform array of helical elements was simulated using CST Microwave Studio and specifically the built-in Time Domain Solver. First, we simulated the performance of the isolated subarrays as these are shown in Fig. 4(a)–(g) and observed the resulting radiation patterns. The arrays were simulated by means of simultaneous excitation with no phase offset so that the main lobe of radiation will be directed toward the array's boresight in all cases and with the individual ports defined as lumped ports with 50-Ω input impedance. Due to the very large electrical size of the array at the high operating frequencies, in order to be able to simulate the arrays, we have employed the hexahedral transmission line method (TLM) mesh option in CST.[1] Note that the computer used for our CST simulations has a 64-bit operating system with 512-GB RAM and a 2.1-GHz processor with 2×24 cores, which should be sufficient for running accurate simulations of such electrically large structures.

The simulated design and the measurement setup can be seen in Fig. 5(a) and (b), respectively, where the fabricated multihyperuniform array is shown in the inset of Fig. 5(b). Note that before conducting our measurements, we follow the calibration techniques that are suggested by the vector network analyzer (VNA) manufacturer so that all cables are calibrated to have equal phase and amplitude at their ends that are connected to the helical elements. As such, the losses associated with the connection cables are considered and we make sure that all elements are driven with equal amplitude and phase. The array is securely mounted on a rotary table, precisely aligned with the center of the double-polarized feeding horn situated at the opposite end of the anechoic chamber, and we use a 24-port ZNBT-8 VNA from Rhode & Schwartz with a maximum measurement frequency of 8.5 GHz. For higher frequencies and measurement frequencies below 1 GHz, we employed the use of the dual-port MS46322A Anritsu VNA with a maximum measurement frequency of 20 GHz. When employing the dual-port VNA, one element at a time is excited, while the rest are terminated with 50-Ω loads and the measurement process is repeated for each element in the array. Note also that when measuring the radiation properties of the multihyperuniform array, the elements that are not intended to operate at the

[1]It is well known among experienced CST users that the hexahedral TLM mesh option is optimal for simulating sparse electrically large structures since the nonsignificant areas are meshed more coarsely than the significant ones, which helps to reduce the required computational resources and time.

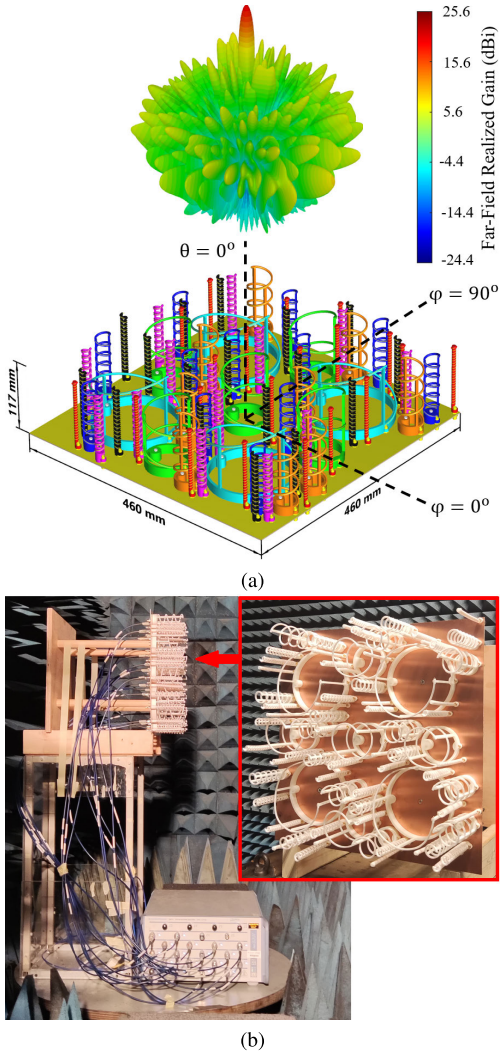

Fig. 5. Multihyperuniform array of helices. (a) Simulated design where the simulated radiation pattern at 12 GHz is shown. The PSLL is at −7.6 dB, the peak backlobe level (PBLL) is at −25.9 dB, and both are calculated taking into account the overall 3-D radiation pattern. (b) Measurement setup with the fabricated array shown in the inset.

measurement bandwidth (out-of-band elements) are terminated to 50-Ω loads.

We first proceeded with measuring the performance of the isolated hyperuniform disordered (Isolated HuD) arrays, as shown in Fig. 4(a)–(g). This was made possible by physically removing the out-of-band elements for each operating bandwidth and measuring the isolated species. The aim of this measurement is to first make sure that the subarrays are operating with satisfactory radiation characteristics and second to compare our measurement results with the simulation results of the isolated hyperuniform arrays. By employing this approach, we are able to guarantee the reliability of the obtained measurement results, thereby establishing a benchmark for our measurement setup. This process is very important since we were unable to simulate the multihyperuniform array for higher frequencies due to unmanageable computational burden and thus following the same experimental process that can guarantee reliable measurement results for the case of the multihyperuniform array.

The measured co-polarized and cross-polarized far-field radiation pattern results for the isolated HuD arrays are shown in Fig. 6 for both principal planes. With respect to Fig. 4, the $\phi = 0°$ and the $\phi = 90°$ planes correspond to the horizontal and vertical planes that cross the center of the array's aperture, respectively. For each species, the measured results are plotted at the corresponding central operating frequency. Note that the 1st, 3rd, 5th and 7th species are right-handed circularly polarized (RHCP), while the rest are left-handed circularly polarized (LHCP), due to the direction of the helical elements windings. As such, the co-polarized and cross-polarized components alternate between the two directions of circular polarization for consecutive species. Note that in order to measure the RHCP and LHCP for each array, we follow the methodology that is presented in [49].

As it can be seen, the cross-polar levels for the 1st species are as low as 5 dB since these helices are comprised by only one turn and increase as the operating frequency increases. This is due to the increase in the number of turns for the higher frequency species with the cross-polar levels reaching up to 30 dB for the 5th species. For the 6th and 7th species, the cross-polar levels slightly decrease to about 20 dB. Note that both the 6th and 7th species helices, which operate for small wavelengths, have many turns and slight wire displacement during the fabrication process, combined with minor misalignments of the helical elements during the measurement process, which can lead to the observed decrease of the cross-polar levels for such small operating wavelengths. Nevertheless, the cross-polar levels are kept over 20 dB for the 2nd species onward.

The simulation as well as measurement results for the Isolated HuD arrays are shown cumulatively in Fig. 7, where the vertical dotted lines indicate the transition between operating bandwidths of consecutive species. In the same plot, the simulated results are given, when the helical elements that form the subarrays are driven with feeds that are optimized to match the antennas to 50 Ω, in order to investigate the effect of the element impedance matching to the multihyperuniform array's radiation pattern behavior. In particular, Fig. 7 illustrates the peak far-field realized gain, axial ratio (AR), peak sidelobe levels (PSLLs), and HPBW for the isolated HuD arrays for all operating frequencies in the 0.4–14-GHz bandwidth. Note that no phase shifting is applied to the excitation ports and all species are designed to radiate toward the array's boresight. As such, for all frequencies, the peak far-field realized gain is situated at the array's boresight and no beam steering is applied. We have measured the radiation properties for both orthogonal planes, and with respect to Fig. 4, the $\phi = 0°$ plane corresponds to the horizontal plane and the $\phi = 90°$ plane corresponds to the vertical plane, whereas $\theta = 0°$ is situated on the array's boresight where the main lobe of radiation is found for all operating frequencies in the 0.4–14-GHz range.

As observed, the peak realized gain values exhibit an upward trend as the operating frequency increases, reaching a maximum measured value of 25.5 dBi. The arrays with optimized feeds have higher gain values compared to the measured arrays, especially for the 4th-to-6th species arrays where a maximum increase of about 4 dB is observed. At the

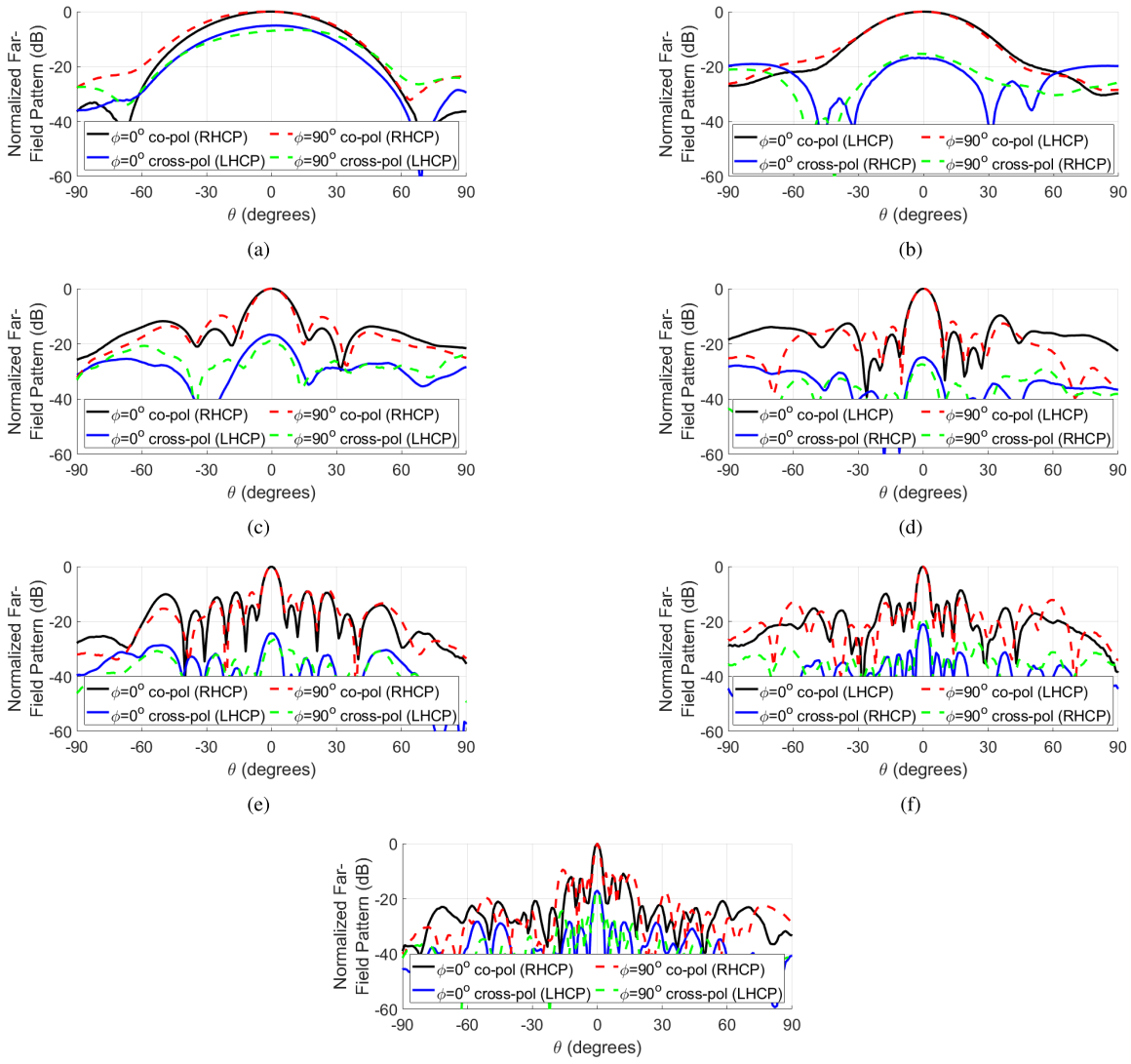

Fig. 6. Measured normalized radiation pattern results for the Isolated HuD arrays shown in Fig. 4(a)–(g) for both principal planes orthogonal to the array aperture. Both the measured co-polarized (black solid line for $\phi = 0°$ and red dotted line for $\phi = 90°$) and cross-polarized (blue solid line for $\phi = 0°$ and green dotted line for $\phi = 90°$) radiation patterns are shown at each species' corresponding central operating frequency. (a) 1st species at 0.7 GHz. (b) 2nd species at 1.4 GHz. (c) 3rd species at 2.3 GHz. (d) 4th species at 3.7 GHz. (e) 5th species at 5.5 GHz. (f) 6th species at 8.2 GHz. (g) 7th species at 12 GHz. RHCP indicates the right-handed circular polarization and LHCP indicates the left-handed circular polarization.

same time, the HPBW is constantly decreasing, reaching a minimum value of around 2° for both planes and for both the case of the measured designs and the simulated ones with optimized feeds. The PSLL values are in most cases fluctuating around −10 dB with the highest value being around −6.3 dB. Nevertheless, all arrays manage to suppress the grating lobes at the corresponding operating bands while maintaining high realized gain and directivity. Furthermore, the measured AR values are below 3 dB for most frequencies, indicating circular polarization. At lower frequencies, the employed elements typically have one or two turns, resulting in increased AR values, as expected. However, at higher frequencies, elements with more turns are used, and this leads to a different behavior with lower AR values. The AR results that are given in Fig. 7(a) reflect the co-polar and cross-polar radiation pattern results that are shown in Fig. 6, where the cross-polar levels between RHCP and LHCP are increasing as the operating frequency increases. In order to measure the AR, we employed the dual-polarized horn that is located at the opposite end of the antenna under test (AUT), and by switching between the two polarizations, we are able to obtain the real and imaginary parts of the transmission to the AUT for both polarizations. Then, by employing the technique presented in [49], we are able to determine the AR of each AUT at the boresight. The measurement and simulation results are matching each other pretty well over the 35:1 operating bandwidth with slight discrepancies at high frequencies being attributed to fabrication inaccuracy and slight misalignment of the elements in the array. These results allow us to follow the same measurement process for the multihyperuniform helical array shown in Fig. 4(h) and obtain convincible results. Furthermore, it is of interest to note that when driving the elements with

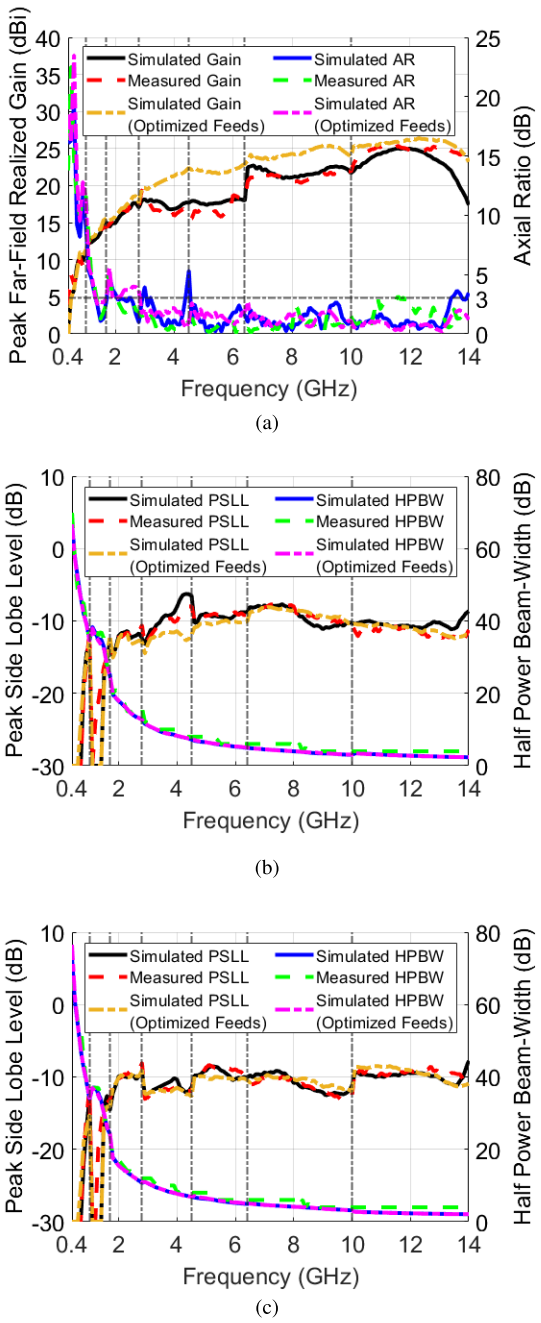

Fig. 7. Measured, simulated, and simulated with optimized feeds radiation pattern results for the seven different Isolated HuD arrays that can be seen in Fig. 4(a)–(g). (a) Peak far-field realized gain and AR where the 3-dB threshold for circular polarization is also shown. (b) PSLL and HPBW for the $\phi = 0°$ plane. (c) PSLL and HPBW for the $\phi = 90°$ plane. The vertical dotted lines indicate the transition between operating bandwidths of consecutive species.

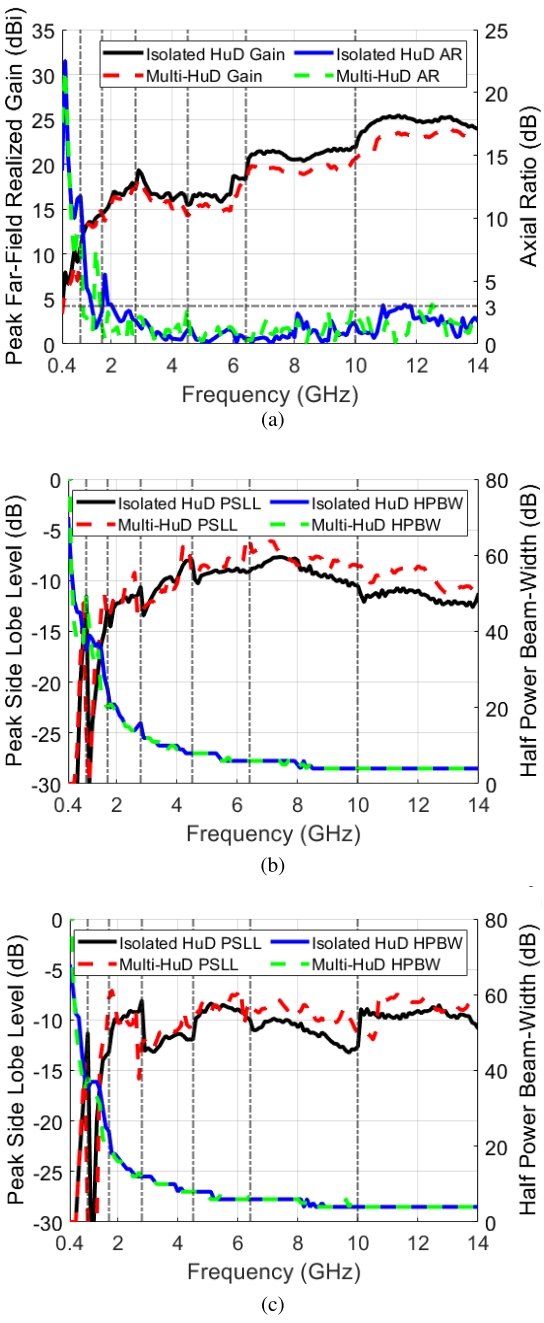

Fig. 8. Measured radiation pattern results for the seven different Isolated HuD arrays that can be seen in Fig. 4(a)–(g) and the multi-HuD antenna array shown in Fig. 4(h). (a) Peak far-field realized gain and AR where the 3-dB threshold for circular polarization is also shown. (b) PSLL and HPBW for the $\phi = 0°$ plane. (c) PSLL and HPBW for the $\phi = 90°$ plane. The vertical dotted lines indicate the transition between operating bandwidths of consecutive species.

optimized feeds, we observe an increase in the peak far-field realized gain and a decrease in the backlobe levels compared to our measured results. On the other hand, the PSLL, AR, and HPBW of the measured arrays and the simulated ones with optimized feeds have almost identical behavior. This is due to the highly directive nature of helical antennas operating in the axial mode and the unique type of distribution that is employed. In turn, this indicates that multihyperuniform disordered (multi-HuD) distributions lead to ultrawideband grating lobe suppression and steadily increasing realized gain values, even for the case when the employed directive elements' RL lies over the usual -10-dB requirement.

As such, we proceed with the testing of the multi-HuD helical antenna array without physically removing the out-of-band species. In this case, the arrays that are not operating in the frequency bandwidth of interest have their elements terminated with 50-Ω loads so that the scattering of the wave due to the out-of-band elements presence can be mitigated

as much as possible. The results of these measurements are shown in Fig. 8, where the already presented Isolated HuD arrays' measurement results are also given for comparison purposes. Observing the peak gain and sidelobe level results and benchmarking them with the Isolated HuD case, we can conclude that the presence of the terminated elements affects the radiation pattern of the array that is excited. In particular, it can be seen that the physical presence of the terminated species reduces the peak gain value of the active species by a maximum of 3 dB while also increasing the sidelobe levels by up to 3.4 dB for some frequencies. This is attributed to the large amount of lossy dielectric material that is present in the multihyperuniform array, as well as the detuning effect that the terminated species have on the active species. As expected, the effects become more pronounced with the increase of the operating frequency since the lossy dielectric materials employed to support the helical antennas lead to undesired scattering of the electromagnetic wave to various directions at these frequencies. Having that in mind, we have fabricated these supporting structures by employing the least amount of dielectric materials possible while maintaining the array's integrity and fabrication accuracy. Furthermore, the employed dielectric has a loss tangent $\tan\delta \approx 0.0046$, which is rather high compared to other commercial dielectric materials. Thus, in future work, we intend to employ a dielectric support material that has lower losses than the one employed here.

Fig. 9 illustrates the simulated radiation pattern results for the Isolated HuD arrays without optimized feeds and the measured radiation pattern results for both the isolated HuD arrays and the multi-HuD array. Specifically, for the sake of brevity, we only show the results at the corresponding central operating frequencies of all seven species for both orthogonal planes. As it can be seen, as the operating frequency increases, the main lobe becomes more and more narrow leading to increased directivity and peak far-field gain values, as shown in Fig. 8. Furthermore, as it was suggested earlier, we observe a very good agreement between the simulated and measured results with respect to the isolated arrays, especially around the main lobe region. This verifies that the measurement process is accurate, and thus, although we could not obtain simulation results for the multihyperuniform array, we are able to trust the obtained measurement results. The results presented in this section indicate that when all the elements are physically present over the same aperture area, the performance of each array deteriorates since the physical presence of the out-of-band elements and the induced mutual coupling will scatter parts of the wave that is radiated by the elements of active species. At the same time, the physical presence of the closely spaced out-of-band elements leads to a slight detuning of the active elements. In turn, this leads to an increase of the PSLL values and, thus, to a reduction of the peak realized gain values, as is evidenced in Fig. 8.

Nevertheless, for all operating frequencies and both ϕ planes, the grating lobes are suppressed with the maximum sidelobe reaching a value of -5.8 dB, which is a 2.8-dB increase compared to the isolated HuD case maximum sidelobe level. The peak realized gain values reach a maximum value of 24 dBi, which is a 1.5-dB drop compared to the isolated HuD case maximum measured gain, whereas the AR has a similar behavior to that of the isolated HuD arrays with circular polarization being achieved over most of the operating frequency band, especially at high frequencies. It is noteworthy to observe that the ascending trend in the peak far-field realized gain values is maintained even when all helical elements are physically incorporated in the shared-aperture antenna array design.

TABLE III

MEASURED PORT-TO-PORT ISOLATION (IN dB) FOR THE MULTIHYPERUNIFORM HELICAL ANTENNA ARRAY. FOR EACH SPECIES AND AT ITS CORRESPONDING OPERATING FREQUENCY BAND (LEFT COLUMN), THE MINIMUM (TOP ROW) AND MAXIMUM (BOTTOM ROW) MEASURED PORT-TO-PORT ISOLATION OVER THE CORRESPONDING FREQUENCY BAND IS GIVEN. THE RESULTS ARE GIVEN FOR HELICAL ANTENNAS BELONGING TO THE SAME, AS WELL AS DIFFERENT SPECIES, INDICATED BY THE SPECIES NUMBER IN THE TOP ROW

Measured port-to-port isolation (dB) between species							
Frequency Band (GHz)	1st	2nd	3rd	4th	5th	6th	7th
1st species	12	13	7	11	7	7	7
$(0.4-1)$	54	60	71	76	82	77	78
2nd species	15	17	15	14	13	15	10
$(1-1.7)$	61	68	72	91	89	81	84
3rd species	17	15	20	12	15	16	10
$(1.7-2.8)$	81	80	80	86	84	96	87
4th species	20	19	16	26	14	15	13
$(2.8-4.5)$	86	97	87	98	94	87	87
5th species	20	19	20	21	26	18	16
$(4.5-6.4)$	86	86	99	87	91	107	99
6th species	21	26	19	21	18	27	17
$(6.4-10)$	74	83	85	77	81	83	102
7th species	26	18	28	27	28	23	31
$(10-14)$	87	98	86	84	96	83	89

In order to evaluate the mutual coupling between elements of the same, as well as of different species, we perform extensive port-to-port isolation measurements between all the elements in the multihyperuniform array distribution shown in Fig. 4(h). As it is understood, there are several different combinations for these measurements since the overall array is made of 80 elements. To that end, we employ the use of the 24-port Rhode & Schwartz VNA and fix one port to one element at a time, while the rest 23 ports are used to measure the port-to-port isolation between this element and all the rest of the elements in the distribution, and we repeat this process for all the elements. Table III tabulates the results of these measurements, and due to the sheer amount of measured data, for each of the seven different operating frequency bands, we provide the average minimum and average maximum measured port-to-port isolation between elements belonging to the same, as well as elements belonging to different species.

As shown in Table III, the isolation between the elements is kept over 10 dB for most cases, with lower isolation values being observed at the operating frequency band of the 1st species and with elements belonging to other species. This

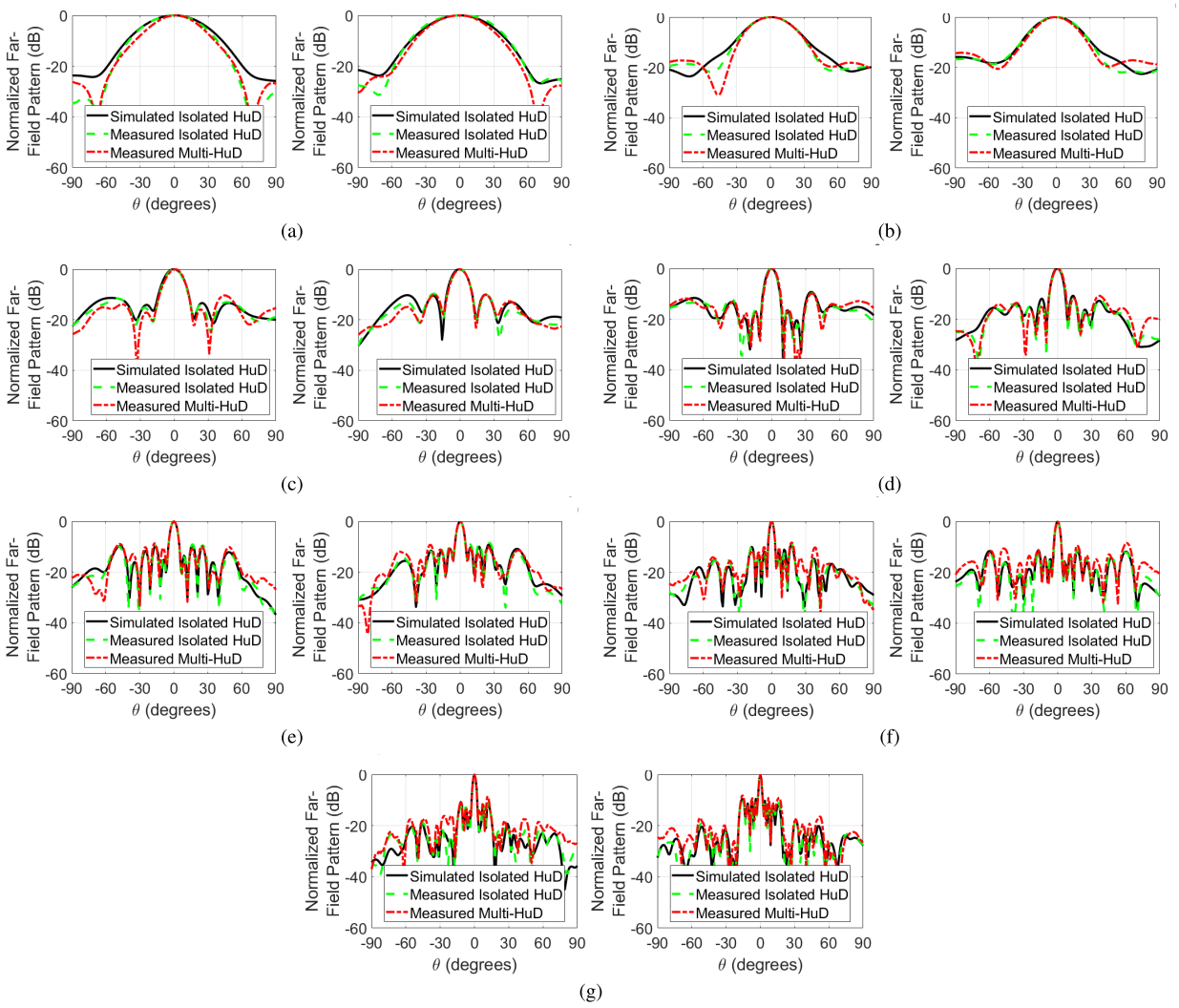

Fig. 9. Simulated normalized radiation pattern results for the Isolated HuD arrays (black solid line) and measured normalized radiation pattern results for the isolated HuD arrays (green dashed line) and the multi-HuD array (red dashed-dotted line) at each species' corresponding central operating frequency. (a) 1st species at 0.7 GHz. (b) 2nd species at 1.4 GHz. (c) 3rd species at 2.3 GHz. (d) 4th species at 3.7 GHz. (e) 5th species at 5.5 GHz. (f) 6th species at 8.2 GHz. (g) 7th species at 12 GHz. For all cases, the left and right figures are for the $\phi = 0°$ and $\phi = 90°$ result, respectively.

is to be expected since, looking at the multihyperuniform distribution in Fig. 4(h), it is evident that many elements belonging to other species are in close proximity to the 1st species elements, due to the dense multihyperuniform distribution of the array's elements. Furthermore, at these operating frequencies (0.4–1 GHz), the interelement spacing between the elements that are in close proximity with the 1st species elements is very narrow compared to the operating wavelength (in some cases even lower than $\lambda/10$). On the other hand, the arrays become sparser with larger spacings, compared to the free-space wavelength as the operating frequency increases, leading to higher isolation between the elements at these frequencies, as evidenced by observing the lower rows of Table III.

V. Comparison With State-of-the-Art Shared-Aperture Antenna Arrays

In order to compare the proposed fabricated and measured antenna array with other similar designs in the existing literature, we focus on comparing several specific performance attributes and radiation pattern properties. In order for the comparison to be fair, we have considered the number of different arrays that make up the shared-aperture array, as well as the central operating frequency of each array. The bandwidth of each array is defined with respect to the 3-dB gain drop from the peak gain that is reported. In addition, we consider the PSLLs for each array at its central operating frequency, along with the corresponding peak realized gain value. Furthermore, the number of elements used in each array design, as well as the thickness of the overall design relative to the wavelength at the central operating frequency, has been considered. It is important to note that there exist previously published works that share a similar foundation by employing hyperuniform disordered distributions in antenna array designs [31], [32]. These works employ a single hyperuniform distribution to design a wideband antenna array and a reflectarray but are both single-band array designs. We compare our work with other multiband shared-aperture antenna

TABLE IV

SHARED-APERTURE ANTENNA ARRAYS STATE-OF-THE-ART COMPARISON. THE FREQUENCY INDICATES THE CENTRAL OPERATING FREQUENCY OF EACH ARRAY. THE PERCENTAGE BANDWIDTH IS CALCULATED WITH REGARD TO THE 3-dB GAIN DROP WITH RESPECT TO THE PEAK GAIN VALUE. CP INDICATES CIRCULAR POLARIZATION, DLP INDICATES DUAL-LINEAR POLARIZATION, SLP INDICATES SINGLE-LINEAR POLARIZATION, LHCP INDICATES THE LEFT-HANDED CIRCULAR POLARIZATION, AND RHCP INDICATES THE RIGHT-HANDED CIRCULAR POLARIZATION. THE THICKNESS OF THE ARRAYS IS CALCULATED IN WAVELENGTHS AT THE CENTRAL OPERATING FREQUENCY OF EACH ARRAY

Ref.	Frequency (GHz)	Bandwidth (%)	PSLL (dB)	Peak Gain (dBi)	No. of elements	Polarization	Thickness (λ)
[7]	5.3; 8.2	21; 21	−12.5; −15	14.5; 17.5	4; 16	CP; CP	0.08; 0.13
[9]	9.6; 14.8; 34.5	3.6; 6.7; 5.1	−11; −15; −12	13.8; 18.1; 19.2	4; 16; 16	DLP; DLP; DLP	0.04; 0.06; 0.15
[10]	20; 29.8;	2.5; 1.7	−12; −11.5	17.7; 21	16; 43	CP; CP	0.7; 1
[11]	5.2; 10;	7.7; 11	NaN; −10.5	10; 12	4; 4	DLP; DLP	0.06; 0.12
[12]	19.7; 29;	18; 12	−12; −14	20; 22	64; 96	CP; CP	2.63; 3.9
[13]	5.7; 14.2;	8.8; 10.6	−13; −15	12.9; 19.3	4; 16	LP; LP	0.14; 0.36
[14]	5.3; 9.6;	4.5; 7.3	−14.5; −15	16.4; 20	1; 4	DLP; DLP	0.9; 1.64
[15]	3.6; 25.8;	25; 1.2	NaN; −11.2	10.9; 22.4	1; 64	SLP; SLP	0.08; 0.59
[17]	0.9; 4;	30; 22.5	−20; −18	8.1; 14	1; 16	DLP; DLP	0.27; 1.22
[20]	1.9; 3.3; 9.5	42.1; 21.2; 10.5	−8; −11; −15	6.3; 14; 21	2; 4; 36	DLP; DLP; DLP	0.29; 0.5; 1.43
[21]	2.2; 3.5; 4.9	45.5; 8.6; 4.1	−12; −11; −13	13.5; 17; 17.8	4; 8; 8	DLP; DLP; DLP	0.26; 0.42; 0.59
This work	0.7; 1.4; 2.3; 3.7; 5.5; 8.2; 12	85.7; 50; 47.8; 46; 34.5; 43.9; 33.3	−24.4; −14.2; −10.4; −9.9; −8.6; −8.3; −8.2;	7; 13; 16.1; 15.4; 14.9; 19; 23.1	4; 5; 9; 12; 14; 17; 20	SLP; LHCP; RHCP; LHCP; RHCP; LHCP; RHCP	0.27; 0.55; 0.9; 1.44; 2.14; 3.19; 4.67

arrays, and since these hyperuniform array designs operate in a single-frequency band, we do not include them in our comparison.

The comparison is shown in Table IV, where the aforementioned attributes are tabulated for different state-of-the-art shared-aperture antenna arrays that can be found in the existing literature. First and foremost, it is evident that the maximum number of different arrays accommodated within the same aperture area in previous studies is three. This limitation arises from the periodic arrangement of the elements and the nonoverlapping condition mentioned earlier. Furthermore, it is worth noting that most of the existing shared-aperture antenna arrays are employing planar elements that are narrowband compared to the helical antenna elements that are employed in this work. As such, it is observed that our array has a fractional bandwidth of at least 33.3% for high operating frequencies and reaches up to an impressive value of 85.7% for low frequencies. On the other hand, most of the reported works have a fractional bandwidth ranging from 2.5% to 12% with some exceptions observed in the works presented in [7], [15], [17], [20], and [21], where the fractional bandwidth can reach up to 45.5% but only for low operating frequencies. In addition, the majority of the reported works have low sidelobe level values ranging from −15 to −11 dB, whereas, in this work, for high frequencies, the sidelobes are around −6 dB, which is a result of the coupling between the out-of-band elements in the shared-aperture array design. Nevertheless, for all operating frequencies, the sidelobes are suppressed and are below −6 dB.

The peak realized gain values that the multihyperuniform shared-aperture antenna array manages to achieve are higher than the ones achieved in reference arrays operating at similar frequencies. It is worth noting that in some of the referenced works, the peak gain values are comparable to the high-frequency gain that is presented here, but with a steep increase in the number of employed elements. In particular, the designs presented in [10], [12], [15], and [20] have peak gain values equal to 21, 22, 22.4, and 21 dBi by employing 43, 96, 64, and 36 elements, respectively. On the other hand, our array achieves a remarkable peak gain value of 23.1 dBi, which stands as the highest among all reference arrays reported so far and is reached with only 20 elements. This is achieved due to its unique hyperuniform disordered distribution that provides increased directivity while being sparse, thus maintaining a low number of employed elements. Finally, most of the reported works employ planar elements, which operate in a narrow bandwidth, and the electrical thickness of these designs varies from 0.04λ to about 0.6λ for most cases. A few exceptions can be found in [12], [14], [17], and [20], where the thickness of the reported works can reach up to 3.9λ. On the other hand, for this work, we employ the wideband nonplanar helical antenna to achieve high peak gain values over a 35:1 bandwidth. It is expected that employing nonplanar elements for a shared-aperture array that operates for such a wide bandwidth leads to increased electrical thickness, especially at the high end of the operating frequency band. This can be observed in this work, where our array's electrical thickness is as low as 0.27λ for low operating frequencies

but reaches up to 4.67λ for high frequencies, which is the highest array electrical thickness among the reported works.

VI. Conclusion and Future Work

In many of the reported works on multiband shared-aperture antenna arrays, the antenna elements were designed so that they can mitigate the out-of-band scattering and thus maintain their radiation pattern attributes even in the physical presence of the out-of-band elements. For this work, we aim to demonstrate a novel approach based on the multihyperuniform distribution. Our results have proven that it is a viable and efficient alternative to conventional methods based on periodic distribution of elements in shared-aperture antenna arrays, and as such, we did not employ any scattering suppression techniques to further optimize the array performance. It is important to note that since the hyperuniform distributions that are employed are nonperiodic distributions, they are naturally robust to element position errors. Of course, the robustness increases with the number of employed elements in each hyperuniform distribution and decreases when a dense multihyperuniform distribution is employed, due to the necessary nonoverlapping condition that is enforced between the elements of different species due to their geometry and dimensions.

Here, we have employed the helical antenna elements for the proof-of-concept, and in the future, we intend to employ planar antenna elements to decrease the array's profile while also applying scattering reduction techniques to implement ultrawideband, steerable, and low-profile planar arrays with multihyperuniform disorder. As such, less out-of-band scattering is expected. However, it should be noted that most planar antenna elements, along with the associated scattering reduction techniques, exhibit narrowband responses. As a result, this approach is likely to restrict the bandwidth of the final design. As such, in the future, it would be of interest to employ a different type of wideband and unidirectional antenna element with lower profile than that of the helical antenna employed in this work. A good candidate for such an implementation is the magnetoelectric dipole antenna that consists of a planar electric dipole combined with a shorted patch antenna [50]. This type of antenna can also be reconfigured for polarization diversity [51], [52]. Furthermore, the magnetoelectric dipole antenna designs that can be found in the associated literature are scalable in most cases and therefore can be designed to operate at different frequency bands.

Moreover, in the future, it would be of interest to fabricate and measure the helical antenna array with multihyperuniform disorder where the elements are driven by optimized feeds and matched to 50 Ω in order to achieve even higher gain values than those reported here. In addition, as future work, we aim to combine the proposed methodology with optimization techniques to jointly optimize the phase and magnitude of the elements along with their positions to further decrease the sidelobe levels and enhance the beam-steering performance of the overall array. Here, our aim is to illustrate a straightforward, fast, and efficient method to optimize multiband array distributions by employing the idea of hyperuniform disorder and more specifically multiple hyperuniform disorder to suppress the sidelobe level for ultrawideband frequencies without having to resort to additional optimization techniques or complicated excitation schemes and amplitude tapering.

To conclude, we have presented here how the idea of multihyperuniformity can be employed in the field of shared-aperture antenna arrays. Taking inspiration from the distribution of photoreceptors on the retina of avian eyes, we have utilized helical antenna elements in a similar manner to mimic the photoreceptor arrangement. This approach aims to achieve wideband unidirectional emission across a broad frequency range of 35:1 using a single design consisting of seven distinct subarrays. The resulting array, which has been successfully fabricated, effectively suppresses grating lobes across the entire frequency spectrum and demonstrates progressively increasing peak far-field realized gain values. Furthermore, the proposed array can be employed as a subarray and scaled up to large arrays of any size by simply repeating them in both directions. Mathematically, it has been proven that the final resulting array is still globally hyperuniform disordered [53]. Finally, the multihyperuniform distribution of elements in a shared-aperture antenna array allows for electromagnetically efficient use of the available space and provides a viable solution to low-profile ultrawideband and small/compact antenna array designs. This work extends the limitations for the realization of multiband antenna arrays, surpassing the previously reported designs that operated in a maximum of three frequency bands. By incorporating optimized disordered distributions within a shared-aperture antenna array design, we have successfully developed ultrawideband array distributions suitable for various scenarios.

References

[1] M. Kragalott, W. R. Pickles, and M. S. Kluskens, "Design of a 5:1 bandwidth stripline notch array from FDTD analysis," *IEEE Trans. Antennas Propag.*, vol. 48, no. 11, pp. 1733–1741, Apr. 2000.

[2] J. Lee, S. Livingston, and R. Koenig, "A low-profile wide-band (5: 1) dual-pol array," *IEEE Antennas Wireless Propag. Lett.*, vol. 2, pp. 46–49, 2003.

[3] B. Munk et al., "A low-profile broadband phased array antenna," in *IEEE Antennas Propag. Soc. Int. Symp., Dig., USNC/CNC/URSI North Amer. Radio Sci. Meeting*, vol. 2, Jun. 2003, pp. 448–451.

[4] M. Jones and J. Rawnick, "A new approach to broadband array design using tightly coupled elements," in *Proc. IEEE Mil. Commun. Conf.*, Oct. 2007, pp. 1–7.

[5] W. F. Moulder, K. Sertel, and J. L. Volakis, "Superstrate-enhanced ultrawideband tightly coupled array with resistive FSS," *IEEE Trans. Antennas Propag.*, vol. 60, no. 9, pp. 4166–4172, Sep. 2012.

[6] D. M. Pozar and S. D. Targonski, "A shared-aperture dual-band dual-polarized microstrip array," *IEEE Trans. Antennas Propag.*, vol. 49, no. 2, pp. 150–157, Feb. 2001.

[7] C.-X. Mao, S. Gao, Y. Wang, Q.-X. Chu, and X.-X. Yang, "Dual-band circularly polarized shared-aperture array for *c*-/*x*-band satellite communications," *IEEE Trans. Antennas Propag.*, vol. 65, no. 10, pp. 5171–5178, Oct. 2017.

[8] K. Naishadham, R. Li, L. Yang, T. Wu, W. Hunsicker, and M. Tentzeris, "A shared-aperture dual-band planar array with self-similar printed folded dipoles," *IEEE Trans. Antennas Propag.*, vol. 61, no. 2, pp. 606–613, Feb. 2013.

[9] C.-X. Mao, S. Gao, Q. Luo, T. Rommel, and Q.-X. Chu, "Low-cost X/Ku/Ka-band dual-polarized array with shared aperture," *IEEE Trans. Antennas Propag.*, vol. 65, no. 7, pp. 3520–3527, Jul. 2017.

[10] X. Chang, H. B. Wang, T. J. Li, S. C. Jin, D. G. Liu, and Y. J. Cheng, "Shared-aperture phased array antenna with codesigned near-field coupled circular polarizer loaded for K/Ka-band wide-angle satellite communication," *IEEE Trans. Antennas Propag.*, vol. 70, no. 9, pp. 7478–7490, Sep. 2022.

[11] C.-X. Mao, S. Gao, Y. Wang, Q. Luo, and Q.-X. Chu, "A shared-aperture dual-band dual-polarized filtering-antenna-array with improved frequency response," *IEEE Trans. Antennas Propag.*, vol. 65, no. 4, pp. 1836–1844, Apr. 2017.

[12] R. S. Hao, J. F. Zhang, S. C. Jin, D. G. Liu, T. J. Li, and Y. J. Cheng, "K-/Ka-band shared-aperture phased array with wide bandwidth and wide beam coverage for LEO satellite communication," *IEEE Trans. Antennas Propag.*, vol. 71, no. 1, pp. 672–680, Jan. 2023.

[13] J. Wu, C. Wang, and Y. X. Guo, "Dual-band co-aperture planar array antenna constituted of segmented patches," *IEEE Antennas Wireless Propag. Lett.*, vol. 19, pp. 257–261, 2020.

[14] F. Qin et al., "A simple low-cost shared-aperture dual-band dual-polarized high-gain antenna for synthetic aperture radars," *IEEE Trans. Antennas Propag.*, vol. 64, no. 7, pp. 2914–2922, Jul. 2016.

[15] T. Li and Z. N. Chen, "Metasurface-based shared-aperture 5G *s*-/*k*-band antenna using characteristic mode analysis," *IEEE Trans. Antennas Propag.*, vol. 66, no. 12, pp. 6742–6750, Dec. 2018.

[16] D. He, Q. Yu, Y. Chen, and S. Yang, "Dual-band shared-aperture base station antenna array with electromagnetic transparent antenna elements," *IEEE Trans. Antennas Propag.*, vol. 69, no. 9, pp. 5596–5606, Sep. 2021.

[17] S. J. Yang, Y. Yang, and X. Y. Zhang, "Low scattering element-based aperture-shared array for multiband base stations," *IEEE Trans. Antennas Propag.*, vol. 69, no. 12, pp. 8315–8324, Dec. 2021.

[18] Y. Li and Q.-X. Chu, "Self-decoupled dual-band shared-aperture base station antenna array," *IEEE Trans. Antennas Propag.*, vol. 70, no. 7, pp. 6024–6029, Jul. 2022.

[19] X. Liu et al., "A mutual-coupling-suppressed dual-band dual-polarized base station antenna using multiple folded-dipole antenna," *IEEE Trans. Antennas Propag.*, vol. 70, no. 12, pp. 11582–11594, Dec. 2022.

[20] K. Li, T. Dong, and Z. Xia, "A broadband shared-aperture L/S/X-band dual-polarized antenna for SAR applications," *IEEE Access*, vol. 7, pp. 51417–51425, 2019.

[21] G.-N. Zhou, B.-H. Sun, Q.-Y. Liang, S.-T. Wu, Y.-H. Yang, and Y.-M. Cai, "Triband dual-polarized shared-aperture antenna for 2G/3G/4G/5G base station applications," *IEEE Trans. Antennas Propag.*, vol. 69, no. 1, pp. 97–108, Jan. 2021.

[22] X. Lu, Y. Chen, S. Guo, and S. Yang, "An electromagnetic-transparent cascade comb dipole antenna for multi-band shared-aperture base station antenna array," *IEEE Trans. Antennas Propag.*, vol. 70, no. 4, pp. 2750–2759, Apr. 2022.

[23] D. He, Y. Chen, and S. Yang, "A low-profile triple-band shared-aperture antenna array for 5G base station applications," *IEEE Trans. Antennas Propag.*, vol. 70, no. 4, pp. 2732–2739, Apr. 2022.

[24] S. Torquato and F. H. Stillinger, "Local density fluctuations, hyperuniformity, and order metrics," *Phys. Rev. E, Stat. Phys. Plasmas Fluids Relat. Interdiscip. Top.*, vol. 68, no. 4, Oct. 2003, Art. no. 041113.

[25] A. Mayer, V. Balasubramanian, T. Mora, and A. M. Walczak, "How a well-adapted immune system is organized," *Proc. Nat. Acad. Sci. USA*, vol. 112, no. 19, pp. 5950–5955, May 2015.

[26] Y. Jiao, T. Lau, H. Hatzikirou, M. Meyer-Hermann, J. C. Corbo, and S. Torquato, "Avian photoreceptor patterns represent a disordered hyperuniform solution to a multiscale packing problem," *Phys. Rev. E, Stat. Phys. Plasmas Fluids Relat. Interdiscip. Top.*, vol. 89, no. 2, Feb. 2014, Art. no. 022721.

[27] A. Gabrielli, M. Joyce, and F. Sylos Labini, "Glass-like universe: Real-space correlation properties of standard cosmological models," *Phys. Rev. D, Part. Fields*, vol. 65, no. 8, Apr. 2002, Art. no. 083523.

[28] A. Gabrielli, B. Jancovici, M. Joyce, J. L. Lebowitz, L. Pietronero, and F. S. Labini, "Generation of primordial cosmological perturbations from statistical mechanical models," *Phys. Rev. D, Part. Fields*, vol. 67, no. 4, Feb. 2003, Art. no. 043506.

[29] B.-Y. Wu, X.-Q. Sheng, and Y. Hao, "Effective media properties of hyperuniform disordered composite materials," *PLoS ONE*, vol. 12, no. 10, Oct. 2017, Art. no. e0185921.

[30] H. Zhang, H. Chu, H. Giddens, W. Wu, and Y. Hao, "Experimental demonstration of Luneburg lens based on hyperuniform disordered media," *Appl. Phys. Lett.*, vol. 114, no. 5, Feb. 2019, Art. no. 053507.

[31] O. Christogeorgos, H. Zhang, Q. Cheng, and Y. Hao, "Extraordinary directive emission and scanning from an array of radiation sources with hyperuniform disorder," *Phys. Rev. Appl.*, vol. 15, no. 1, Jan. 2021, Art. no. 014062.

[32] H. Zhang, W. Wu, Q. Cheng, Q. Chen, Y.-H. Yu, and D.-G. Fang, "Reconfigurable reflectarray antenna based on hyperuniform disordered distribution," *IEEE Trans. Antennas Propag.*, vol. 70, no. 9, pp. 7513–7523, Sep. 2022.

[33] H. Zhang, Q. Cheng, H. Chu, O. Christogeorgos, W. Wu, and Y. Hao, "Hyperuniform disordered distribution metasurface for scattering reduction," *Appl. Phys. Lett.*, vol. 118, no. 10, Mar. 2021, Art. no. 101601.

[34] T. Amoah and M. Florescu, "High-qoptical cavities in hyperuniform disordered materials," *Phys. Rev. B, Condens. Matter*, vol. 91, no. 2, Jan. 2015, Art. no. 020201.

[35] M. Florescu, S. Torquato, and P. J. Steinhardt, "Complete band gaps in two-dimensional photonic quasicrystals," *Phys. Rev. B, Condens. Matter*, vol. 80, no. 15, Oct. 2009, Art. no. 155112.

[36] W. Man et al., "Photonic band gap in isotropic hyperuniform disordered solids with low dielectric contrast," *Opt. Exp.*, vol. 21, no. 17, p. 19972, 2013.

[37] L. S. Froufe-Pérez et al., "Role of short-range order and hyperuniformity in the formation of band gaps in disordered photonic materials," *Phys. Rev. Lett.*, vol. 117, no. 5, Jul. 2016, Art. no. 053902.

[38] R. Degl'Innocenti et al., "Hyperuniform disordered terahertz quantum cascade laser," *Sci. Rep.*, vol. 6, no. 1, pp. 1–7, Jan. 2016.

[39] M. Castro-Lopez, M. Gaio, S. Sellers, G. Gkantzounis, M. Florescu, and R. Sapienza, "Reciprocal space engineering with hyperuniform gold disordered surfaces," *APL Photon.*, vol. 2, no. 6, Jun. 2017, Art. no. 061302.

[40] R. D. Batten, F. H. Stillinger, and S. Torquato, "Classical disordered ground states: Super-ideal gases and stealth and equi-luminous materials," *J. Appl. Phys.*, vol. 104, no. 3, Aug. 2008, Art. no. 033504.

[41] S. Torquato, G. Zhang, and F. H. Stillinger, "Ensemble theory for stealthy hyperuniform disordered ground states," *Phys. Rev. X*, vol. 5, no. 2, May 2015, Art. no. 021020.

[42] O. Christogeorgos, E. Okon, and Y. Hao, "A computational model for generating multihyperuniform distributions for realistic antenna array and metasurface designs," *EPJ Appl. Metamater.*, vol. 11, p. 5, Jan. 2024.

[43] O. U. Uche, F. H. Stillinger, and S. Torquato, "Constraints on collective density variables: Two dimensions," *Phys. Rev. E, Stat. Phys. Plasmas Fluids Relat. Interdiscip. Top.*, vol. 70, no. 4, Oct. 2004, Art. no. 046122.

[44] J. D. Kraus, "The helical antenna," *Proc. IRE*, vol. 37, no. 3, pp. 263–272, 1949.

[45] R. Stegen, "Impedance matching of helical antennas," *IEEE Trans. Antennas Propag.*, vol. AP-12, no. 1, pp. 125–126, Jan. 1964.

[46] H. Nakano, Y. Samada, and J. Yamauchi, "Axial mode helical antennas," *IEEE Trans. Antennas Propag.*, vol. AP-34, no. 9, pp. 1143–1148, Sep. 1986.

[47] A. Boothby, R. Hwang, V. Das, J. Lopez, and D. Y. C. Lie, "Design of axial-mode helical antennas for Doppler-based continuous non-contact vital signs monitoring sensors," in *Proc. IEEE Radio Wireless Symp.*, Jan. 2012, pp. 87–90.

[48] H. Mardani, N. Buchanan, R. Cahill, and V. Fusco, "Impedance matching of axial mode helical antennas," *WSEAS Trans. Circuits Syst.*, vol. 20, pp. 66–69, May 2021.

[49] B. Yen Toh, R. Cahill, and V. F. Fusco, "Understanding and measuring circular polarization," *IEEE Trans. Educ.*, vol. 46, no. 3, pp. 313–318, Aug. 2003.

[50] L. Ge and K. M. Luk, "A low-profile magneto-electric dipole antenna," *IEEE Trans. Antennas Propag.*, vol. 60, no. 4, pp. 1684–1689, Apr. 2012.

[51] F. Wu and K.-M. Luk, "A reconfigurable magneto-electric dipole antenna using bent cross-dipole feed for polarization diversity," *IEEE Antennas Wireless Propag. Lett.*, vol. 16, pp. 412–415, 2017.

[52] L. Ge, X. Yang, D. Zhang, M. Li, and H. Wong, "Polarization-reconfigurable magnetoelectric dipole antenna for 5G Wi-Fi," *IEEE Antennas Wireless Propag. Lett.*, vol. 16, pp. 1504–1507, 2017.

[53] O. Leseur, R. Pierrat, and R. Carminati, "High-density hyperuniform materials can be transparent," *Optica*, vol. 3, no. 7, p. 763, 2016.

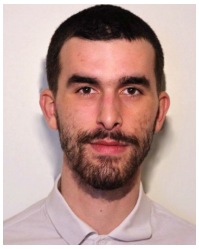

Orestis Christogeorgos received the B.Sc. and M.Sc. degrees in electrical and computer engineering from the Aristotle University of Thessaloniki, Thessaloniki, Greece, in 2018, and the Ph.D. degree in electronic engineering from the Queen Mary University of London, London, U.K., in 2024.

He is currently working as a Post-Doctoral Research Assistant at the Queen Mary University of London. He has published four journal articles and four conference papers and has presented at several scientific conferences. His current research interests include the design and fabrication via 3-D printing of novel aperiodic antenna arrays and shared-aperture antenna arrays by employing hyperuniform disordered distributions. Other research interests include the design and prototyping of metasurfaces for scattering reduction and the design and fabrication of lens antennas.

Dr. Christogeorgos was a recipient of the 2019 Young Scientist Best Paper Award at the International Conference on Electromagnetics in Advanced Applications (IEEE-ICEAA).

Ernest Okon (Member, IEEE) received the B.Sc. and M.Sc. degrees in electrical engineering from the University of Lagos, Lagos, Nigeria, in 1992 and 1996, respectively, and the Ph.D. degree in electronic engineering from King's College London, London, U.K., in 2001.

He has over 30 years of experience in electromagnetic modeling and antenna design. He has held a teaching appointment at Kings College London from 1997 to 2001 and a visiting appointment at the University of Bedfordshire, Luton, U.K., from 2010 to 2014, where he taught courses on computational electromagnetics, antennas, and communication systems. He joined the BAE Systems Advanced Technology Centre, Chelmsford, U.K., as a Research Engineer from 2001 to 2007 working on electromagnetic modeling and antenna design. In 2007, he joined the Aerospace Division, Thales U.K., Crawley, U.K., as a Principal Antenna Engineer and is currently a Thales Expert working on electromagnetic modeling and antenna design. His experience is in the design of microwave and millimeter-wave antennas for electronic warfare, radar, and communication systems. He also has experience in radar cross section measurement and modeling. This encompasses design, electromagnetic modeling, and measurement of antenna elements; printed antennas; radomes; polarization twisters; active integrated antennas; and phased array antennas. He has designed antennas for ground, air, sea, and space platforms. He has contributed to NATO working groups on radar cross section. He also has numerous publications on antennas.

Dr. Okon has received several industry awards for innovation. He is a Chartered Engineer registered with the U.K. Engineering Council and a member of the Institution of Engineering and Technology (IET). He is active in review activities on antenna-related publications.

Yang Hao (Fellow, IEEE) received the Ph.D. degree in computational electromagnetics from the Centre for Communications Research, University of Bristol, Bristol, U.K., in 1998.

He was a Post-Doctoral Research Fellow with the School of Electronic, Electrical and Computer Engineering, University of Birmingham, Birmingham, U.K. He is currently a Professor of antennas and electromagnetics with the Antenna Engineering Group, Queen Mary University of London, London, U.K. His research has been recognized both nationally and internationally through his books *Antennas and Radio Propagation for Body-Centric Wireless Communications* and *FDTD Modeling of Metamaterials: Theory and Applications* (Artech House, USA) and highly cited articles published in leading journals, including *Nature Communications*, *Advanced Science*, *Physical Review Letters*, *Applied Physics Letters*, PROCEEDINGS OF THE IEEE, and IEEE TRANSACTIONS.

Dr. Hao is an Elected Fellow of the Royal Academy of Engineering and Institution of Engineering and Technology (IET). He has won many accolades, including the Prestigious AF Harvey Prize in 2015, the BAE Chairperson Silver Award in 2014, and the Royal Society Wolfson Research Merit Award in 2013. He was a Strategic Advisory Board Member of EPSRC, where he is committed to championing RF/microwave engineering for reshaping the future of U.K. manufacturing and electronics. He received the EurAAP Antenna Award in 2024 for world-leading contributions in wireless communications.